# 3D SEGMENTATION OF VESSELS BY INCREMENTAL IMPLICIT POLYNOMIAL FITTING AND CONVEX OPTIMIZATION

*Andreas Biesdorf*[1], *Stefan Wörz*[1], *Hendrik von Tengg-Kobligk*[2], *Karl Rohr*[1], *and Christoph Schnörr*[3]

[1]Dept. Bioinformatics and Functional Genomics, Biomedical Computer Vision Group, University of Heidelberg, BIOQUANT, IPMB, and DKFZ Heidelberg, Germany
[2]Institute of Diagnostic, Interventional and Pediatric Radiology, University Hospital of Bern
[3] University of Heidelberg, Image and Pattern Analysis Group, Heidelberg, Germany

## ABSTRACT

Robust and accurate segmentation of blood vessels is important for treatment and diagnosis of cardiovascular diseases. Here, we introduce a new approach for 3D segmentation of vessels which is formulated as a convex parameter estimation problem and combined with an incremental tracking approach. Parameter values are determined as global optimum of a semidefinite program and admissible shape variations are imposed by convex constraints. The performance of the approach has been evaluated using 3D synthetic images and clinical 3D CTA images of the aorta including pathologies.

## 1. INTRODUCTION

Pathologies of the aorta are a major cause of death in western countries that can be diagnosed using, for example, computed tomography angiography (CTA) and can be treated by minimally-invasive placement of an endovascular graft (EVG). To minimize the risks associated with this treatment option, an EVG should be chosen based on the individual anatomy of each patient. For therapy planning, individual morphological parameters such as diameters and length of a pathology of the aorta are important, which can be determined by segmentation approaches. A wide spectrum of approaches for vessel segmentation exists, including approaches based on differential measures (e.g., [1, 2]), minimal paths (e.g., [3]), and deformable models (e.g., [4, 5, 6, 7]).

Approaches based on deformable models using parametric intensity models have the advantage that prior knowledge about the vessel shape and the intensity structure can be exploited (e.g., [4, 5, 7]). However, these approaches are formulated as a non-linear, least-squares parameter estimation problem. As a consequence, the objective function is *non-convex*. In this contribution, we introduce a new approach for 3D vessel segmentation in tomographic image data which uses incremental implicit polynomial fitting and *convex* optimization. The approach is based on the observation that the tubular shape of a vessel can be described locally by an implicit quadratic function. Given that the set of 3D tubular shapes with arbitrary orientation and variation within natural bounds forms a convex set, we demonstrate that the problem of estimating the local shape of a vessel can be approximated by a convex objective function. To segment vessels from 3D image data, we have combined the convex optimization method with an incremental tracking scheme. Our approach has been evaluated based on 3D synthetic and clinical 3D CTA images of the aorta, and the performance has been quantified as well as compared with a previous approach.

## 2. LOCAL IMPLICIT POLYNOMIAL FITTING

Given a local image region $V \subset \mathbb{R}^3$, we wish to estimate the shape of a region $\Omega \subset V$ that optimally separates a tubular structure from the background. To this end, we use a parametric model $f(\mathbf{x}; p),\ p \in \{p_0, p_1\}$ that denote the intensity variations. We assume that $f$ is a piecewise constant function taking only two values $p_0$ and $p_1$ to describe the foreground and background intensity, respectively:

$$d(\mathbf{x}; p) := \big(f(\mathbf{x}, p_0) - g(\mathbf{x})\big)^2 - \big(f(\mathbf{x}, p_1) - g(\mathbf{x})\big)^2, \quad (1)$$

where $g(\mathbf{x})$ denotes the image intensities. If the parametric model $f(\mathbf{x}; p)$ represents $g(\mathbf{x})$ well, then $d(\mathbf{x}; p) \leq 0$ if $\mathbf{x} \notin \Omega$ and $d(\mathbf{x}; p) \geq 0$ if $\mathbf{x} \in \Omega$. Consequently, any function $s(\mathbf{x})$, that maximizes the functional $\sum_{\mathbf{x} \in V} d(\mathbf{x}; p) s(\mathbf{x})$should have the same sign as $d(\mathbf{x})$ and the zero level set $\{\mathbf{x} \colon s(\mathbf{x}) = 0\}$ will indicate the shape of $\Omega$. To determine the local shape of a vessel, we maximize the functional over a family of quadratic functions whose zero level sets correspond to tubular shapes:

$$s(\mathbf{x}; \mathcal{A}) := \big\langle \mathbf{x} - \mathbf{a}, \mathbf{A}(\mathbf{x} - \mathbf{a}) \big\rangle + a_0, \quad \mathcal{A} = \{\mathbf{A}, \mathbf{a}, a_0\}, \quad (2)$$

where $\mathbf{A}$ is a $3 \times 3$ matrix which describes the shape, $\mathbf{a}$ is a vector which represents the translation, and $a_0$ is a scalar which denotes a scale factor of the model. Convexity of the shape is ensured by restricting possible shape variations to a convex set $C_{\mathcal{A}}$ of shape parameters $\mathcal{A} \in C_{\mathcal{A}}$.

Note that tubular surfaces can be represented by symmetric matrices $\mathbf{A}$ with ordered eigenvectors $\boldsymbol{\lambda}(\mathbf{A})$ contained in

the convex set $\boldsymbol{\lambda}_l \leq \boldsymbol{\lambda}(\mathbf{A}) \leq \boldsymbol{\lambda}_u, \quad \boldsymbol{\lambda}_l, \boldsymbol{\lambda}_u \in \mathbb{R}^3$, where the inequalities hold elementwise. Vectors $\boldsymbol{\lambda}_l, \boldsymbol{\lambda}_u$ are fixed vectors that specify lower and upper bounds for the maximum admissible deformation of a straight cylinder. The first two components of $\boldsymbol{\lambda}_l$ and $\boldsymbol{\lambda}_u$ are equal and specify the same strictly positive interval, whereas the third component defines a symmetric interval around $\mathbf{0}$.

Our specification of admissible shape variations is based on the following proposition: *Let* $\mathbf{A}, \mathbf{B} \in \mathcal{S}_+^3$ *and suppose* $\mathbf{A} \succeq \mathbf{B}$. *Then* $\boldsymbol{\lambda}(\mathbf{A}) \geq \boldsymbol{\lambda}(\mathbf{B})$. Here, $\mathcal{S}_+^n$ denotes the convex cone of $n \times n$ positive semidefinite symmetric matrices and $\mathbf{A} \succeq \mathbf{B}$ means that $\mathbf{A} - \mathbf{B}$ is symmetric positive semidefinite. Note that the monotonicity property follows from the classical min-max principle characterizing the eigenvalues of symmetric matrices [8]. Thus, convexity may be imposed by

$$\mathbf{A} - \mathrm{Diag}(\boldsymbol{\lambda}_l) \succeq 0, \quad \mathrm{Diag}(\boldsymbol{\lambda}_u) - \mathbf{A} \succeq 0. \tag{3}$$

Since the conditions in (3) require affine mappings of $\mathbf{A}$ to lie in the convex cone $\mathcal{S}_+^3$ and as convexity is preserved under affine mappings, the set $C_A := \{\mathbf{A} \in \mathcal{S}_+^3 \colon \mathbf{A} \text{ satisfies (3)}\}$ is given by the intersection of convex sets, hence is convex. Thus, feasible solutions are contained in $C_{\mathcal{A}} := C_A \times \mathbb{R}^3 \times \mathbb{R}$.

Locations $\mathbf{x} \in V$ with $s(\mathbf{x}; \mathcal{A}) \approx 0$ should dominate the sensitivity of the functional with respect to variations of $\mathcal{A}$. However, this is not the case for the squared distance function in (1), where locations far from the zero level set will have the highest influence on the functional. To reduce the influence of large residuals far from the zero level set, we use an apodization function $\phi_\sigma(t) = \big(1 + \exp(-t/\sigma)\big)^{-1}$, parametrized by a scale parameter $\sigma$. Note that $\phi_\sigma$ is log-concave and that the logarithm is a strictly monotone function. Thus, applying the logarithm to $\phi_\sigma$ convexifies the problem without changing the optimum of $\phi_\sigma$. By transforming the maximization into a minimization problem we obtain the objective function

$$J(\mathcal{A}) = -\sum_{\mathbf{x} \in V} \log\Big(\phi_\sigma\big(d(\mathbf{x}; p) s(\mathbf{x}; \mathcal{A})\big)\Big), \mathcal{A} \in C_{\mathcal{A}}, \tag{4}$$

with $d(\cdot)$ and $s(\cdot)$ defined by (1) and (2), respectively.

### 2.1. Convex Approximation

The objective function in (4) can be written as

$$J(\mathcal{A}) = -\sum_{\mathbf{x} \in V} \log\Big(\phi_\sigma\big(r(\mathbf{x}; \mathcal{A})\big)\Big), \tag{5}$$

where $r(\mathbf{x}; \mathcal{A}) = d(\mathbf{x}; p) s(\mathbf{x}; \mathcal{A})$. Since $\phi_\sigma$ is log-concave, the function $\psi := -\log \phi_\sigma$ is convex. Moreover, since $\psi$ is nonincreasing, the objective function is convex if $r(\mathbf{x}; \mathcal{A})$ is concave. This holds, in particular, if $r(\mathbf{x}; \mathcal{A})$ is linear in $\mathcal{A}$. Consequently, by linearization of $r(\mathbf{x}; \mathcal{A})$, we obtain a convex approximation of the objective function which is used to iteratively estimate the shape parameters numerically. With $\mathcal{A} = \mathcal{A}' + \delta\mathcal{A}$, we have

$$\begin{aligned} s(\mathbf{x}; \mathcal{A}) &= s(\mathbf{x}; \mathcal{A}' + \delta\mathcal{A}) \\ &= \langle \mathbf{x}, \mathbf{A}\mathbf{x} \rangle - 2\langle \mathbf{x}, \mathbf{A}\mathbf{a} \rangle + \langle \mathbf{a}, \mathbf{A}\mathbf{a} \rangle + a_0 \\ &= s(\mathbf{x}; \mathcal{A}') + \langle \mathbf{x}\mathbf{x}^\top - 2\mathbf{x}\mathbf{a}'^\top + \mathbf{a}'\mathbf{a}'^\top, \delta\mathbf{A} \rangle \\ &\quad + \langle \delta\mathbf{a}, 2\mathbf{A}'^\top(\mathbf{a}' - \mathbf{x}) \rangle + \delta a_0 \\ &\quad + \langle \delta\mathbf{a}, (\mathbf{A} + \delta\mathbf{A})\, \delta\mathbf{a} \rangle + 2\langle \delta\mathbf{a}, \delta\mathbf{A}\, (\mathbf{a}' - \mathbf{x}) \rangle \\ &=: s(\mathbf{x}; \mathcal{A}') + s_c(\mathbf{x}; \mathcal{A}) + s_{nc}(\mathbf{x}; \mathcal{A}), \end{aligned} \tag{6}$$

where $s_c(\mathbf{x}; \mathcal{A})$ and $s_{nc}(\mathbf{x}; \mathcal{A})$ represent the convex and nonconvex parts, respectively. With small increments $\|\delta\mathbf{A}\| \leq \varepsilon$, $\|\delta\mathbf{a}\| \leq \varepsilon$, the nonconvex part becomes negligible. As a result, the convex approximation reads

$$J_c(\mathcal{A}) := \sum_{\mathbf{x} \in V} \log\Big(\frac{1}{1 + c(\mathcal{A}') \exp\big(-d_\sigma(\mathbf{x}; p) s_c(\mathbf{x}; \mathcal{A})\big)}\Big),$$

where $d_\sigma(\mathbf{x}; p) := d(\mathbf{x}; p)/\sigma$, and $c(\mathcal{A}') := \exp\big(-d_\sigma(\mathbf{x}; p) s(\mathbf{x}; \mathcal{A}')\big)$.

### 2.2. Algorithm

We iteratively compute parameter updates $\mathcal{A} = \mathcal{A}' + \delta\mathcal{A}$ by solving at each iteration the semidefinite program

$$\min_{\delta\mathcal{A}} J_c(\mathcal{A}) \quad \text{subject to} \quad \mathcal{A} \in C_{\mathcal{A}}. \tag{7}$$

In each iteration, we compute

$$\mathcal{A} \leftarrow \Pi_{C_{\mathcal{A}}}(\mathcal{A}' + \delta\mathcal{A}), \qquad \delta\mathcal{A} = -\tau \nabla_{\delta\mathcal{A}} J_c(\mathcal{A}), \tag{8}$$

with small increments $\tau$ until convergence. Note that $\Pi_{C_{\mathcal{A}}}(\mathcal{A}' + \delta\mathcal{A})$ denotes the projection of $\mathcal{A}' + \delta\mathcal{A}$ to the convex constraints. The projection is computed by decomposition of the symmetric matrix $\mathbf{A}' + \delta\mathbf{A} = \mathbf{Q}\mathbf{D}\mathbf{Q}^T$, where $\mathbf{D} = \mathrm{Diag}(\boldsymbol{\lambda}(\mathbf{A}' + \delta\mathbf{A}))$ with eigenvalues $\boldsymbol{\lambda}(\mathbf{A}' + \delta\mathbf{A})$ and $\mathbf{Q}$ denotes the matrix with the corresponding eigenvectors. If the eigenvalues $\boldsymbol{\lambda}(\mathbf{A}' + \delta\mathbf{A})$ do not agree with the constraints, they are projected to the constraint boundaries. By doing this, we obtain a new diagonal matrix $\mathbf{D}_\Pi \leftarrow \Pi_{C_{\mathcal{A}}}(\mathbf{D})$, which serves to compute $\mathbf{A} = \mathbf{Q}\mathbf{D}_\Pi\mathbf{Q}^T$.

## 3. INCREMENTAL 3D VESSEL SEGMENTATION

Our approach for 3D vessel segmentation determines local vessel parameters incrementally along the path of a vessel. We have developed an incremental approach, which consists of three main steps: (i) initialization, (ii) estimation of local model parameters using convex optimization, and (iii) tracking along the centerline.

For *initialization*, coarse estimates for the starting point ($\mathbf{x}_0$), the local orientation ($\boldsymbol{\alpha}_0$), the radius of the region-of-interest ($R_{ROI}$) for model fitting, as well as for the local background ($p_0$) and foreground intensities ($p_1$) are required. Note

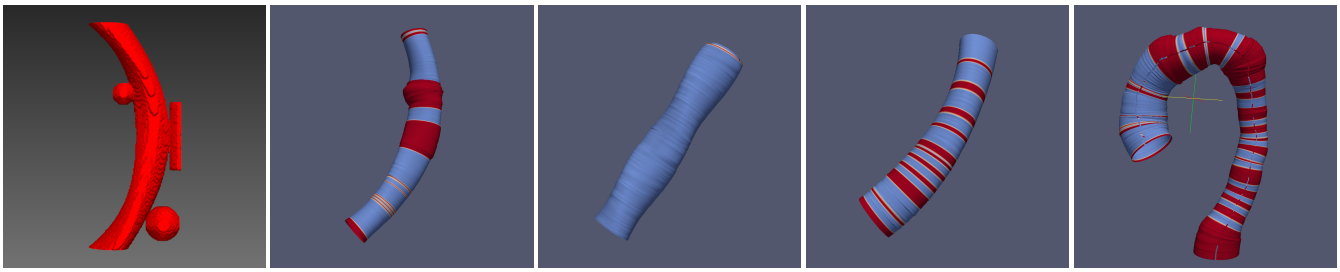

(a) (b) (c) (d) (e)

**Fig. 1**. Segmentation results for 3D image data. (a) 3D original image and (b) segmentation result of a section of a twisted torus with neighboring structures. (c) Segmentation result for a 3D synthetic image of a twisted cylinder and (d) for a section of a twisted torus. (e) Segmentation result a clinical 3D CTA image. Colors indicate regions where the constraints were active (red).

that this information has to be provided only once for initialization of the first vessel segment. In our case, we determine these parameters semi-automatically based on two points of the centerline and the vessel radius. For subsequent vessel segments, updates for $R_{ROI}$, $p_0$ and $p_1$ are determined based on the segmentation result of the previous vessel segment.

For *estimation of local model parameters*, the convex objective function (7) is minimized in a 3D ROI around a vessel ($R_{ROI} = c_{ROI} \cdot D_{max}/2$, $c_{ROI} = 1.2$). For minimization, a projected gradient descent approach is used and parameter updates are iteratively computed. The parameters $p_0$ and $p_1$ are determined in each iteration using the current segmentation result and the mean intensities of the background and foreground intensities in the ROI.

For *incremental tracking* along the vessel centerline, we predict a new 3D position based on the estimated centerline position $\mathbf{x}_k = (x_1, x_2, x_3)_k$ and the local 3D orientation $\boldsymbol{\alpha}_k = (\alpha, \beta, \gamma)_k$ of the current vessel segment. To this end, we compute the current vessel centerline position $\mathbf{x}_k$ based on the center of the ROI $\mathbf{x}_{0,k}$ and the translation $\mathbf{a}_k$ by $\mathbf{x}_k = \mathbf{x}_{0,k} - \mathbf{a}_k$. The orientation $\boldsymbol{\alpha}_k$ of a vessel segment can be determined based on the eigenvectors and corresponding eigenvalues of the projected estimates $\mathbf{A} = \mathbf{Q}\mathbf{D}_\Pi\mathbf{Q}^T$ (see Sect. 2 above). Given the ordered eigenvalues $|\lambda_1| \leq |\lambda_2| \leq |\lambda_3|$ of $\mathbf{A}$, the orientation of the current vessel is given by the eigenvector $\boldsymbol{\phi}_1$ corresponding to the eigenvalue $\lambda_1$. To predict a new center position $\mathbf{x}_{k+1}$,we compute $\mathbf{x}_{k+1} = \mathbf{x}_k - \tau\boldsymbol{\phi}_1$, where $\tau$ denotes the step size. The two remaining eigenvectors $\boldsymbol{\phi}_2$ and $\boldsymbol{\phi}_3$ span a plane which is orthogonal to the vessel centerline and indicate the rotation of the quadratic surface around $\boldsymbol{\phi}_1$. Note that a 2D orthogonal cross-section of a quadratic surface can be described by an ellipse with a major and minor axis. The orientation of the minor axis is given by the eigenvector $\boldsymbol{\phi}_2$, while the orientation of the major axis corresponds to the eigenvector $\boldsymbol{\phi}_3$. In our clinical application the minimum and maximum vessel diameters along the vessel are important parameters, which can be determined by $D_{min} = 2\sqrt{\frac{-a_0}{\lambda_2}}$ and $D_{max} = 2\sqrt{\frac{-a_0}{\lambda_3}}$, respectively.

## 4. EXPERIMENTAL RESULTS

### 4.1. Convergence analysis

In a first experiment, we have studied the convergence of our approach based on the $L_2$-norm of the gradient of $J_c$ and using different clinical 3D CTA images. We found that the approach typically converges after 10 to 30 iterations.

### 4.2. Evaluation based on 3D synthetic images

To evaluate the effect of neighboring structures, we have generated 3D synthetic image data of a section of a twisted torus with spherical and boxlike structures in the vicinity of a vessel. In Fig. 1a, the shape of the vessel and the neighboring structures are shown. The neighboring structures have different sizes, shapes, and distances to the vessel. The segmentation result of our new approach is shown in Fig. 1b. Colors indicate regions where the constraints were active (red) at convergence. From the colors it can be seen that all structures in the vicinity of the vessel have an effect on the segmentation result (constraints are active). However, only one structure with a direct connection to the vessel (i.e., Fig. 1a, top left sphere) has a notable influence on the segmentation result.

We have applied the new approach to 150 3D synthetic images of a twisted cylinder and 100 3D images showing a section of a twisted torus with elliptical cross-sections. In Fig. 1c,d, typical segmentation results for both sets of images are shown. To quantify the segmentation accuracy, we have computed mean errors for clinically relevant parameters comprising the minimum, mean, and maximum vessel diameters, $\overline{e}_{D_{min}}$, $\overline{e}_{D_{mean}}$, and $\overline{e}_{D_{max}}$, respectively, as well as the mean error for the centerline position $\overline{e}_{\mathbf{x}_0}$ and the mean Dice coefficient $\overline{d}$. Table 1 shows the results of the new approach compared to a previous model-based approach [5]. For both sets of synthetic images, we obtain similar results. For $D_{min}$ and $D_{max}$, the accuracy of the new approach is significantly higher than that of the previous approach. In comparison to the previous approach, the new approach yields an improvement of $73\% - 87\%$ for $D_{min}$ and $D_{max}$. For $D_{mean}$, the

**Table 1**. 3D synthetic image data: Mean errors and standard deviations for the diameters $D_{min}$, $D_{mean}$, and $D_{max}$, for the centerline position $\mathbf{x}_0$, as well as the mean and the standard deviation of the Dice coefficent $\overline{d}$ for different approaches.

| Accuracy / Approach | 150 twisted cylinders | | | | | 150 twisted tori | | | | |
|---|---|---|---|---|---|---|---|---|---|---|
| | $\overline{e}_{D_{min}}$ | $\overline{e}_{D_{mean}}$ | $\overline{e}_{D_{max}}$ | $\overline{e}_{\mathbf{x}_0}$ | $\overline{d}$ | $\overline{e}_{D_{min}}$ | $\overline{e}_{D_{mean}}$ | $\overline{e}_{D_{max}}$ | $\overline{e}_{\mathbf{x}_0}$ | $\overline{d}$ |
| Prev. approach [5] | $3.14_{\pm 0.83}$ | $0.29_{\pm 0.20}$ | $3.93_{\pm 1.32}$ | $0.10_{\pm 0.01}$ | $0.91_{\pm 0.02}$ | $3.12_{\pm 0.72}$ | $0.35_{\pm 0.19}$ | $4.03_{\pm 1.16}$ | $0.02_{\pm 0.00}$ | $0.91_{\pm 0.02}$ |
| New approach | $0.86_{\pm 0.88}$ | $0.33_{\pm 0.40}$ | $0.83_{\pm 0.17}$ | $0.01_{\pm 0.01}$ | $0.96_{\pm 0.01}$ | $0.82_{\pm 0.96}$ | $0.43_{\pm 0.52}$ | $0.54_{\pm 0.05}$ | $0.14_{\pm 0.02}$ | $0.97_{\pm 0.01}$ |

accuracy of the previous approach is slightly higher. For the centerline position $\mathbf{x}_0$ we obtain similar good results for the new and the previous approach with a subvoxel accuracy of $\mathbf{x}_0 \leq 0.11$ voxels. For $\overline{d}$, the new approach yields the best results with $\overline{d} = 0.96$ and $\overline{d} = 0.97$, respectively.

### 4.3. Segmentation results for 10 3D CTA images

We have also applied the approach to 10 different clinical 3D CTA images including pathologies. The images were acquired with a 16-slice CT scanner (Acquilion 16, Toshiba, Japan) using iodinated contrast media (Imeron, 400 mgI/ml and Iomeprol, 400 mgI/ml) and comprise between 597 and 758 slices with a spacing of 0.8 mm. Each slice consists of $512 \times 512$ voxels with a resolution of 0.51 - 0.63 mm/voxel. In Fig. 1e, the segmentation result for an example image is shown. From the figure it can be seen that the approach successfully segments the vessel for a difficult clinical case. We have also performed a quantitative comparison with a previous model-based approach [5] (see Tab. 2). For $D_{mean}$, $\mathbf{x}_0$, and $\overline{d}$ we obtain similar good results for both approaches with subvoxel accuracy, while for $D_{min}$ and $D_{max}$ we obtain more accurate results for the new approach.

## 5. CONCLUSIONS

In this contribution, we introduced for the first time a 3D vessel segmentation approach based on implicit polynomials and convex optimization, and we combined the approach with an incremental tracking scheme. Our approach was applied to 3D synthetic and 3D clinical image data of the aorta and the performance was quantitatively compared with a previous model-based approach. Overall, it turned out that while we obtain similar good results for the mean diameter, the centerline position and the Dice coefficient $d$, the new approach outperforms the previous approach for the minimum and maximum diameters.

**Table 2**. 3D CTA image data: Mean errors and standard deviations for the diameters $D_{min}$, $D_{mean}$, and $D_{max}$, for the centerline position $\mathbf{x}_0$, as well as the mean and the standard deviation of the Dice coefficent $d$ for different approaches.

| Approach | Ten 3D CTA images | | | | |
|---|---|---|---|---|---|
| | $\overline{e}_{D_{min}}$ | $\overline{e}_{D_{mean}}$ | $\overline{e}_{D_{max}}$ | $\overline{e}_{\mathbf{x}_0}$ | $\overline{d}$ |
| Prev. appr. | $2.66_{\pm 0.62}$ | $0.91_{\pm 0.35}$ | $1.57_{\pm 0.35}$ | $0.88_{\pm 0.10}$ | $0.97_{\pm 0.00}$ |
| New appr. | $1.82_{\pm 0.38}$ | $0.95_{\pm 0.29}$ | $1.22_{\pm 0.30}$ | $0.90_{\pm 0.16}$ | $0.97_{\pm 0.01}$ |

## 6. REFERENCES


[1] A.F. Frangi, W.J. Niessen, K.L. Vincken, and M.A. Viergever, "Multiscale vessel enhancement filtering," in *Proc. MICCAI'98*, Cambridge, MA/USA, Oct. 1998, vol. 1496 of *LNCS*, pp. 130–137, Springer Berlin Heidelberg.

[2] S. Cetin, A. Demir, A. Yezzi, M. Degertekin, and G. Unal, "Vessel tractography using an intensity based tensor model with branch detection," *IEEE Trans. on Medical Imaging*, vol. 32, no. 2, pp. 348–363, 2013.

[3] P. Lo, B. van Ginneken, and M. de Bruijne, "Vessel Tree Extraction using Locally Optimal Paths," in *Proc. 7th IEEE Internat. Symposium on Biomedical Imaging: From Nano to Macro (ISBI'10)*, Rotterdam, The Netherlands, April 2010, IEEE Computer Society.

[4] H.J. Noordmans and A.W.M. Smeulders, "High accuracy tracking of 2D/3D curved line structures by consecutive cross-section matching," *Pattern Recogn. Lett.*, vol. 19, no. 1, pp. 97–111, 1998.

[5] S. Wörz, H. von Tengg-Kobligk, V. Henninger, F. Rengier, H. Schumacher, D. Böckler, H.-U. Kauczor, and K. Rohr, "3D Quantification of the Aortic Arch Morphology in 3D CTA Data for Endovascular Aortic Repair," *IEEE Trans. on Biomed. Eng.*, vol. 57, no. 10, pp. 2359–2368, 2010.

[6] K. Hameeteman, R. van Klooster, M. Selwaness, A. van der Lugt, J.C.M. Witteman, W.J. Niessen, and S. Klein, "Carotid wall volume quantification from magnetic resonance images using deformable model fitting and learning-based correction of systematic errors," *Physics in Med and Biol*, vol. 58, no. 5, pp. 1605, 2013.

[7] A. Biesdorf, K. Rohr, T. Müller, T.F. Weber, T. Heye, W. Hosch, H. von Tengg-Kobligk, and S. Wörz, "Segmentation and quantification of the aortic arch using joint 3D model-based segmentation and elastic image registration," *Med Im Anal*, vol. 16, no. 6, pp. 1187–1201, 2012.

[8] E. Fischer, "Über quadratische Formen mit reellen Koeffizienten," *Monatshefte für Math*, vol. 16, no. 1, 1905.